PHYSICAL REVIEW A **87**, 042517 (2013)

Dynamic polarizabilities for the low-lying states of Ca$^+$

Yong-Bo Tang,[1,2] Hao-Xue Qiao,[1] Ting-Yun Shi,[2] and J. Mitroy[3,*]
[1]*Department of Physics, Wuhan University, Wuhan 430072, People's Republic of China*
[2]*State Key Laboratory of Magnetic Resonance and Atomic and Molecular Physics, Wuhan Institute of Physics and Mathematics, Chinese Academy of Sciences, Wuhan 430071, People's Republic of China*
[3]*School of Engineering, Charles Darwin University, Darwin, Northern Territory 0909, Australia*
(Received 20 March 2013; published 29 April 2013)

The dynamic polarizabilities of the $4s$, $3d$, and $4p$ states of Ca$^+$, are calculated using a relativistic structure model. The wavelengths at which the Stark shifts between different pairs of transitions are zero are computed. Experimental determination of the magic wavelengths can be used to estimate the ratio of the $f_{3d_J \to 4p_{J'}}$ and $f_{4s_{1/2} \to 4p_{J'}}$ oscillator strengths. This could prove valuable in developing better atomic structure models and, in particular, lead to improved values of the polarizabilities needed in the evaluation of the blackbody radiation shift of the Ca$^+$ ion.

DOI: 10.1103/PhysRevA.87.042517 PACS number(s): 31.15.ac, 31.15.ap, 34.20.Cf

I. INTRODUCTION

The dynamic polarizability of an atom or ion gives a measure of the energy shift of the atom or ion when immersed in an electromagnetic field [1–3]. For any given state, one can write

$$\Delta E = -\tfrac{1}{2}\alpha_d(\omega)F^2, \tag{1}$$

where $\alpha_d(\omega)$ is the polarizability of the quantum state at frequency ω, and F is a measure of the strength of the ac electromagnetic field. The value of the dynamic polarizability in the $\omega \to 0$ limit is the static dipole polarizability.

The magic wavelength for a transition is the wavelength for which the ac Stark shift of the transition energy is zero [4–7]. The identification of magic wavelengths and their use in making optical lattices has resulted in the development of optical lattice clocks which have the potential to exceed the performance characteristics of the existing standard for time, namely the cesium microwave clock [8–12].

However, the experimental determination of magic wavelengths also provides valuable information to constrain the atomic structure models that are used to estimate the impact of Stark shifts on the performance of atomic and ion clocks [13,14]. A parameter related to the magic wavelength is the tune-out wavelength. The tune-out wavelengths for an atomic state are the wavelengths at which the polarizability for that state goes to zero [15–17]. It should be noted that most atomic states have a number of tune-out wavelengths just like most atomic transitions have a variety of magic wavelengths.

The advantage of magic and tune-out wavelength measurements are that they are effectively null experiments. They measure the frequencies at which polarizability related quantities are equal to zero. Therefore, they do not rely on a precise determination of the strength of a static electric field or the intensity of a laser field. This makes it possible to determine the magic wavelengths to a high degree of precision [9,18–22].

There have been a number of theoretical studies of the properties of the low-lying Ca$^+$ ion [23–29] by three different research groups. One of these groups [24] used a nonrelativistic approach while the other two groups used explicitly relativistic formulations [26–29]. One of the singular features about the relativistic calculations are significant differences between predictions of the properties of spin-orbit doublets. The relativistic all-order many-body perturbation theory method predicts relatively small nongeometric differences between the line strengths of the $3d_J$ and $4p_J$ spin-orbit doublets [23,29]. The relativistic coupled cluster approach typically gives much larger differences [26]. One of the secondary aims of the present work is to shed light on these differences.

The present paper reports calculations of the dynamic polarizabilities of the five lowest states of Ca$^+$. The Hamiltonian used is a fully relativistic version of a semiempirical fixed core potential that has been successfully applied to the description of many one- and two-electron atoms [30–33]. While there are many differences in the technical detail, the underlying philosophy and the effective Hamiltonian for the valence electron are essentially the same once the relativistic modifications are taken into account. Magic wavelengths for the $4s \to 3d_{3/2,5/2}$ and $4s \to 4p_{1/2,3/2}$ transitions are given. The dynamic polarizability of the ground Ca$^+(4s)$ state is dominated by the $4s \to 4p_J$ transitions and its accuracy is largely dependent on the accuracy of the transition matrix elements connecting the $4s$ and $4p_J$ states. The description of transitions involving the Ca$^+(3d)$ state is complicated by the effect that the $3d$ electron has on the core electrons. The $3d$ orbitals have the smallest $\langle r \rangle$ expectation values of any of the valence electrons and this does distort the wave functions for the outermost core electrons [34,35]. One consequence of this is greater uncertainty in the calculation of transition matrix elements involving the $3d_J$ states [27,29,35]

All results reported in this paper are given in atomic units with the exception of the lifetimes, which are given in seconds. The value adopted for the speed of light is $c = 137.035\,999\,074(44)$ a.u.

II. FORMULATION AND ENERGIES

A. Solution of the Dirac-Fock equation for closed shell atomic system

The calculation methodology is as follows. The first step involves a Dirac-Fock (DF) calculation of the Ca^{2+} ground

---

[*] jxm107@physics.anu.edu.au

state. The DF calculation begins with the equation

$$\left(\sum_{i}^{N} H_D(\boldsymbol{r}_i) + \sum_{i<j}^{N} \frac{1}{r_{ij}}\right) \psi(\boldsymbol{r}) = E\psi(\boldsymbol{r}), \tag{2}$$

where H_D is the single-electron Dirac Hamiltonian

$$H_D(\boldsymbol{r}_i) = c\boldsymbol{\alpha} \cdot \boldsymbol{p} + c^2(\beta - 1) + V(r_i), \tag{3}$$

where c is the speed of light, $\boldsymbol{p}$ is the momentum operator, and $\boldsymbol{\alpha}$ and β are the Dirac matrices [36].

The orbitals of the DF wave function, $\psi(r)$, can be written as

$$\psi(\boldsymbol{r}) = \frac{1}{r}\begin{pmatrix} g_{n\kappa}(r)\Omega_{\kappa m}(\hat{r}) \\ i f_{n\kappa}(r)\Omega_{-\kappa m}(\hat{r}) \end{pmatrix}, \tag{4}$$

where $g_{n\kappa}(r)$ and $f_{n\kappa}(r)$ are the large and small components, respectively, $\Omega_{\kappa m}(\hat{r})$ and $\Omega_{-\kappa m}(\hat{r})$ correspond to the angular components. The radial Dirac equation for an orbital can be expressed schematically as

$$\begin{pmatrix} V(r) + V_{\mathrm{DF}}(r) & -c\left(\frac{d}{dr} - \frac{\kappa}{r}\right) \\ c\left(\frac{d}{dr} + \frac{\kappa}{r}\right) & -2c^2 + V(r) + V_{\mathrm{DF}}(r) \end{pmatrix} \begin{pmatrix} g_{n\kappa}(r) \\ f_{n\kappa}(r) \end{pmatrix}$$
$$= \varepsilon \begin{pmatrix} g_{n\kappa}(r) \\ f_{n\kappa}(r) \end{pmatrix}, \tag{5}$$

where V_{DF} is called the DF potential and $V(r)$ is the interaction potential between the electron and the nucleus. A Fermi nuclear distribution approximation is usually adopted for many-electron atomic systems.

The single-particle orbitals are written as linear combinations of analytic basis functions and so the method of Roothaan [37,38] is used to recast the DF equations into a set of matrix equations. The functions chosen are B-splines with Notre Dame boundary conditions [39]. The large and small components are expanded in terms of a B-spline basis of k order defined on the finite cavity $[0, R_{\max}]$,

$$g_{n\kappa}(r) = \sum_{i=1}^{N} C_i^{g,n} B_{i,k}(r), \tag{6}$$

$$f_{n\kappa}(r) = \sum_{i=1}^{N} C_i^{f,n} B_{i,k}(r). \tag{7}$$

The finite cavity is set as a knots sequence, $\{t_i\}$, satisfying an exponential distribution [40,41]. The specifics of the grid were that $R_{\max} = 60a_0$ and 50 B-splines of order $k = 7$ were used to represent the single-particle states. Using the Galerkin method and MIT-bag-model boundary conditions [39], the DF equations were solved by iteration until self-consistency was achieved. The single-electron orbital (Koopmans) energies of the closed shell Ca^{2+} ion agreed with those computed with the GRASP92 program [42] to better than 10^{-5} a.u.

B. Polarization potential

The effective potential of the valence electron with the core is then written

$$V_{\mathrm{core}} = V_{\mathrm{dir}}(\mathbf{r}) + V_{\mathrm{exc}}(\mathbf{r}) + V_{\mathrm{pol}}(\mathbf{r}). \tag{8}$$

TABLE I. Theoretical and experimental energy levels (in Hartree) for some of the low-lying states of Ca^{+}. The energies are given relative to the energy of the Ca^{2+} core. The experimental data were taken from the NIST tabulation [43].

Level	DF	DFCP	Experiment [43]
$4s_{1/2}$	−0.416 631 5	−0.436 277 7	−0.436 277 6
$3d_{3/2}$	−0.330 869 5	−0.374 083 4	−0.374 082 7
$3d_{5/2}$	−0.330 759 7	−0.373 807 4	−0.373 806 2
$4p_{1/2}$	−0.309 998 6	−0.321 496 6	−0.321 496 6
$4p_{3/2}$	−0.309 088 9	−0.320 481 8	−0.320 481 0
$5s_{1/2}$	−0.193 315 8	−0.198 348 6	−0.198 587 6
$4d_{3/2}$	−0.168 738 3	−0.175 153 6	−0.177 298 9
$4d_{5/2}$	−0.168 664 1	−0.175 062 2	−0.177 211 4
$5p_{1/2}$	−0.156 765 6	−0.160 317 8	−0.160 468 8
$5p_{3/2}$	−0.156 432 9	−0.160 061 2	−0.160 112 3

The direct and exchange interactions of the valence electron with the DF core were calculated exactly. The ℓ-dependent polarization potential, V_{pol}, was semiempirical in nature with the functional form

$$V_{\mathrm{pol}}(r) = -\sum_{\ell j} \frac{\alpha_{\mathrm{core}} g_{\ell j}^2(r)}{2r^4} |\ell j\rangle\langle \ell j|. \tag{9}$$

The coefficient, α_{core} is the static dipole polarizability of the core and $g_{\ell j}^2(r) = 1 - \exp\left(-r^6/\rho_{\ell,j}^6\right)$ is a cutoff function designed to make the polarization potential finite at the origin. The static dipole polarizability core was set to $\alpha_{\mathrm{core}} = 3.26$ a.u. [29]. The cutoff parameters, $\rho_{\ell,j}$, were tuned to reproduce the binding energies of the ns ground state and the np_J, nd_J excited states. Values of the cutoff parameters are $\rho_{0,1/2} = 1.7419a_0$, $\rho_{1,1/2} = 1.6389a_0$, $\rho_{1,1/2} = 1.6354a_0$, $\rho_{2,3/2} = 1.8472a_0$, and $\rho_{2,3/2} = 1.8489a_0$. The cutoff parameters for $\ell \geqslant 3$ were set to a common value of $1.897a_0$. Table I gives the calculated B-spline and experimental energies coming from [43]. The calculations with the core-polarization potential are identified as the Dirac-Fock plus core polarization (DFCP) model. Differences between DFCP and experimental energies mostly occur in the fourth digit after the decimal point.

One of the interesting aspects of Table I concerns the spin-orbit splitting of the $4p_J$ and $5p_J$ states. The polarization potential parameters $\rho_{1,1/2}$ and $\rho_{1,3/2}$ were tuned to give the correct spin-orbit splitting of the $4p_J$ states. Making this choice resulted in the spin-orbit splittings for the $5p_J$ states also being very close to experimental values.

III. TRANSITION MATRIX ELEMENTS AND ASSOCIATED QUANTITIES

A. Reduced matrix elements

The dipole matrix elements were computed with a modified transition operator [30,44,45], e.g.,

$$r\mathbf{C}^1 = r\mathbf{C}^1 - [1 - \exp(-r^6/\rho^6)]^{1/2} \frac{\alpha_{\mathrm{core}} r\mathbf{C}^1}{r^3}. \tag{10}$$

The cutoff parameter, ρ used in Eq. (10) was set to $\rho = (\rho_{\ell_a,j_a} + \rho_{\ell_b,j_b})/2$ where a,b refer to the initial and final states of the transition.

TABLE II. Comparison of the electric dipole (E1), electric quadrupole (E2) reduced matrix elements of several interested states of the Ca$^+$ ion.

Transition	DFCP	MBPT-SD	RCC
		Dipole	
$4s_{1/2}-4p_{1/2}$	2.879	2.898(13) [29]	2.88(1) [26]
$4s_{1/2}-4p_{3/2}$	4.073	4.099(18) [29]	4.03(1) [26]
$4s_{1/2}-5p_{1/2}$	0.089		
$4s_{1/2}-5p_{3/2}$	0.109		
$3d_{3/2}-4p_{1/2}$	2.500	2.464(16) [29]	2.40(2) [26]
$3d_{3/2}-4p_{3/2}$	1.116	1.100(6) [29]	1.09(1) [26]
$3d_{5/2}-4p_{3/2}$	3.356	3.306(18) [29]	3.22(4) [26]
$3d_{3/2}-5p_{1/2}$	0.091		
$3d_{3/2}-5p_{3/2}$	0.044		
$3d_{5/2}-5p_{3/2}$	0.131		
$3d_{3/2}-4f_{5/2}$	1.964	1.927(52) [29]	
$3d_{5/2}-4f_{5/2}$	0.526	0.516(6) [29]	
$3d_{5/2}-4f_{7/2}$	2.354	2.309(29) [29]	
$4p_{1/2}-5s_{1/2}$	2.081	2.073(11) [29]	
$4p_{1/2}-3d_{3/2}$	4.205	4.28(3) [29]	
$4p_{3/2}-4d_{3/2}$	1.894	1.93(1) [29]	
$4p_{3/2}-4d_{5/2}$	5.675	5.78(3) [29]	
		Quadrupole	
$4s_{1/2}-3d_{3/2}$	8.120	7.939(37) [23]	7.973 [54]
			8.12(5) [55]
$4s_{1/2}-3d_{5/2}$	9.964	9.740(47) [23]	9.979 [54]
			9.97(6) [55]

The static quadrupole polarizability of the Ca^{2+} core is needed for the calculation of the lifetimes of the $3d_J$ states. It was set $\alpha_{q,\text{core}} = 6.936$ a.u. [46].

There have been a number of previous calculations of reduced matrix elements and polarizabilities for the low-lying states of Ca$^+$. The semiempirical configuration interaction plus core polarization (CICP) can be regarded as a nonrelativistic predecessor of the present calculation [24,30]. Another method used is the relativistic all-order single-double method where all single and double excitations of the DF wave function are included to all orders of many-body perturbation theory (MBPT-SD) [27,29,47]. There have also been calculations using the relativistic coupled cluster (RCC) method [26]. The RCC and MBPT-SD approaches have many common features [48–50]. Atomic parameters computed using the RCC approach have on a number of occasions had significant differences with independent calculations [29,51–53].

The reduced matrix elements between the various low-lying states are the dominant contributor to the polarizabilities of the $4s$, $3d$, and $4p$ levels. These are given in Table II and compared with the results from other recent calculations. The ratio of line strengths for spin-orbit doublets is also interesting to tabulate since they can reveal the extent to which dynamical effects (as opposed to geometric effects caused by the different angular momenta) are affecting the matrix elements. Some line strength ratios are given in Table III.

The variation among the DFCP, MBPT-SD, and RCC matrix elements listed in Table III does not exceed 5%. The DFCP matrix elements are usually closer to the MBPT-SD calculations than the RCC matrix elements. A better indication of the differences between the DFCP, MBPT-SD and RCC calculations is gained by examination of the line strength ratios listed in Table III. The DFCP line strength ratios are within 1% of the values that would be expected simply due to the angular momentum factors alone. The ratios are in very good agreement with the MBPT-SD ratios. It should be noted, that the line strength ratios for the resonant transition of potassium have been measured to be very close to 2.0 [17] and DFCP and MBPT-SD calculations also predict line strength ratios very close to 2.0 [17,56].

TABLE III. Comparison of the line strengths ratios for transitions involving various spin-orbit doublets. The notation $4s_{1/2}-4p_{3/2:1/2}$ means the line strength ratio defined by dividing $4p_{3/2}$ line strength by the $4p_{1/2}$ line strength.

Transition	DFCP	MBPT-SD	RCC
$4s_{1/2}-4p_{3/2:1/2}$	2.0014	2.001 [29]	1.958(17) [26]
$4s_{1/2}-5p_{3/2:1/2}$	1.4990		
$3d_{3/2}-4p_{3/2:1/2}$	5.0182	5.02 [29]	4.85(12) [26]
$4p_{3/2}-3d_{5/2:3/2}$	9.043	9.04 [29]	8.73(27) [26]
$4s_{1/2}-3d_{5/2:3/2}$	1.5057	1.5052 [29]	1.5665 [54]
			1.5075 [55]
$4p_{3/2}-4d_{5/2:3/2}$	5.0181		
$4p_{3/2}-4d_{5/2}$	9.021		

By way of contrast, RCC matrix element ratios exhibit about 4% differences from the geometric ratios. One would expect the RCC matrix element ratios to be much closer to the MBPT-SD ratio given the close formal similarities between the RCC and MBPT-SD approaches. The RCC matrix element ratios listed in Table III also show significant differences from the geometric ratio for the $4s \rightarrow 3d_J$ transitions. The DFCP and MBPT-SD ratios lie within 1% of the geometric ratios. It should be noted that a similar situation exists for the $5s - 4d_{5/2:3/2}$ line strength ratios of Sr$^+$ with RCC calculations exhibiting much larger differences due to nongeometric effects than other calculations [57]. The feature common to the DFCP and MBPT-SD methods is that they use large B-spline basis sets and calculated quantities are expected to be independent of basis set effects. One possible cause for the different RCC matrix element ratios lies in the Gaussian basis set used to represent virtual excitations in the RCC calculation. This point will be addressed later where polarizabilities are discussed.

TABLE IV. Lifetime of the $3d_{3/2}$ and $3d_{5/2}$ levels of Ca$^+$ (in s). The $3d_{3/2} : 3d_{5/2}$ lifetime ratio is also given.

Source	$\tau_{3d_{3/2}}$	$\tau_{3d_{5/2}}$	Ratio
DFCP	1.143(1)(s)	1.114(1)	1.0260
MBPT-SD [29]	1.196(1)(s)	1.165(11)	1.0266
RCC [26]	1.185(7)	1.110(9)	1.0675
MCHF [34]	1.160	1.140	1.0175
Experiment [23]	1.176(11)	1.168(7)	1.007(15)
Experiment [58]	1.17(5)	1.09(5)	1.073(90)
Experiment [59]	1.064(17)		
Experiment [60]	1.111(46)	0.994(38)	1.118(80)

TABLE V. Lifetimes (in ns) of the $4p_{\frac{1}{2}}$ and $4p_{\frac{3}{2}}$ states. The $4p_{\frac{1}{2}} : 4p_{\frac{3}{2}}$ lifetime ratio is also given. The quantity R gives the fraction of the total decay rate arising from the indicated transition.

Level	DFCP	MBPT-SD [29]	RCC [26]	Expt.
$4p_{\frac{1}{2}}(ns)$	6.94(1)	6.88(6)	6.931	7.098(20) [66] 7.07(7) [67]
$4p_{\frac{3}{2}}(ns)$	6.75(1)	6.69(6)	6.881	6.926(19) [66] 6.87(6) [67] 6.72(2) [68] 6.61(30) [69]
$R(4p_{\frac{1}{2}}-4s_{\frac{1}{2}})$	0.9324		0.9374(74)	
$R(4p_{\frac{1}{2}}-3d_{\frac{3}{2}})$	0.0676		0.0626(5)	
$R(4p_{\frac{3}{2}}-4s_{\frac{1}{2}})$	0.9313	0.9340	0.9350(62)	0.9347(3) [70]
$R(4p_{\frac{3}{2}}-3d_{\frac{3}{2}})$	0.0069	0.006 67	0.006 66(4)	0.006 61(4) [70]
$R(4p_{\frac{3}{2}}-3d_{\frac{5}{2}})$	0.0617	0.0593	0.0583(4)	0.0587(2) [70]
Ratio	1.0281	1.0284	1.0073	1.025(3) [66] 1.029(14) [67]

B. Lifetimes

The two most important lifetimes for the Ca^+ clock [61–65] are the lifetimes of the $3d_J$ and $4p_J$ levels. The $3d_J$ states decay to the ground state in an electric quadrupole transition with lifetime of about 1.1 s [23]. The $4p_J$ states experience electric dipole transitions to both the $3d_J$ and $4s$ states. Table IV gives the lifetimes of the $3d_J$ states while Table V gives the lifetimes of the $4p_J$ states. All DFCP lifetimes were computed using experimental energy differences.

The most recent experiment for the $3d_J$ lifetimes give a ratio of 1.007 ± 0.015 s for the $3d_{3/2}$ and $3d_{5/2}$ states. This suggests that the $4s \rightarrow 3d_J$ matrix element ratios should be close to the values expected from angular momentum coupling considerations. Older experiments [58,60] give ratios further from unity, but in these cases the uncertainties are much larger.

The lifetimes of the $4p_J$ states depend on two transitions, these are the $4s-4p_J$ and $3d_{J'}-4p_J$ transitions, with the $4s-4p_J$ transition being the most important. The lifetimes and branching ratios for the $4p_J$ states are given in Table V. It is not possible to reconcile the theoretical and experimental lifetimes at the 1% level. The two most recent experiments [66,67] gave lifetimes that are 2% larger than the DFCP lifetimes and 3% larger than the MBPT-SD lifetimes. Older Hanle effect experiments [68,69] gave lifetimes closer to the MBPT-SD and DFCP lifetimes.

Measurements of the branching ratios of the $4p_{3/2}$ state yield a picture where the MBPT-SD calculations largely agree with experiment while the DFCP tends to overestimate the contributions of the decays to the $3d_J$ levels. Another area of partial agreement between theory and experiment occurs for the $4p_{1/2} : 4p_{3/2}$ lifetime ratio. The DFCP, MBPT-SD, and experimental ratios range from 1.025 to 1.030, with the RCC calculation again providing an outlier at 1.0073.

IV. POLARIZABILITIES

A. Static polarizabilities

The static dipole and quadrupole polarizabilities are calculated by the usual sum rule

$$\alpha_{(\ell)} = \sum_i \frac{f_{gi}^{(\ell)}}{\varepsilon_{gi}^2}, \tag{11}$$

where the $f_{gi}^{(\ell)}$ are the absorption oscillator strengths and ε_{gi} is the excitation energy of the transition. Static dipole polarizabilities for the $4s$, $4p_J$, and $3d_J$ states are listed in Table VI. All polarizabilities were computed using experimental energy differences.

TABLE VI. Dipole and quadrupole polarizabilities (in a.u.) for low-lying states of the Ca^+ ion. Nonrelativistic quadrupole polarizabilities are not given for states with $\ell > 0$. The RCC-STO results are those from Ref. [26] that used a Slater-type orbital basis to represent virtual excitations.

	$\alpha_1^{(0)}$		$\alpha_1^{(t)}$		α_2	
State	DFCP	Others	DFCP	Others	DFCP	Others
$4s_{1/2}$	75.28	76.1(5) MBPT-SD [29] 75.49 CICP [24] 73.0(1.5) RCC [26] 75.3(4) f-sums [72] 74.3 RCC-STO [26]			882.43	871(4) MBPT-SD [29] 875.1 CICP [24] 712.9(24) RCC [71] 906(5) RCC [55]
$4p_{1/2}$	−2.774	−0.75(70) MBPT-SD [29] −2.032 CICP [24]			7.466[4]	
$4p_{3/2}$	−0.931	1.02(64) MBPT-SD [29] −2.032 CICP [24]	10.12	10.31(28) MBPT-SD [29] 10.47 CICP [24]	−3.571[4]	
$3d_{3/2}$	32.99	32.0(3) MBPT-SD [29] 32.73 CICP [24] 28.5(1.0) RCC [26] 31.6 RCC-STO [26]	−17.88	−17.43(23) MBPT-SD [29] −17.64 CICP [24] −15.87 RCC [26] −17.7 RCC-STO [26]	4928	
$3d_{5/2}$	32.81	31.8(3) MBPT-SD [29] 32.73 CICP [24] 29.5(1.0) RCC [26] 32.5 RCC-STO [26]	−25.16	−24.51(29) MBPT-SD [29] −25.20 CICP [24] −22.49(5) RCC [26] −25.5 RCC-STO [26]	−3304	−3706(75) RCC [55]

TABLE VII. The contributions of individual transitions to the polarizabilities of the $4s_{1/2}$ and $4p_{1/2}$ states at the magic wavelengths. The numbers in parentheses are uncertainties in the last digits of the energy or wavelength calculated by introducing 2% uncertainties into the most important matrix elements.

ω (a.u.) λ (nm)	0 ∞	0.065 956 1(11 247) 690.817(11.984)	0.115 298 1(4) 395.1807(14)	0.123 809 1(303) 368.0149(901)
		$4s_{1/2}$		
$4p_{1/2}$	24.0704	35.9364	−2665.2940	−147.2228
$5p_{1/2}$	0.0097	0.0102	0.0117	0.0121
$4p_{3/2}$	47.7532	70.6856	5558.6017	−333.5265
$5p_{3/2}$	0.0145	0.0153	0.0175	0.0181
Remainder	0.1672	0.1710	0.1794	0.1815
Core	3.2600	3.2664	3.2793	3.2823
Total	75.2751	110.0849	2896.7954	−477.2554
		$4p_{1/2}$		
$4s_{1/2}$	−24.0704	−35.9364	2665.2940	147.2228
$5s_{1/2}$	11.7449	16.4949	97.8655	−798.9861
$3d_{3/2}$	−39.6152	69.1092	10.4051	8.7196
$4d_{3/2}$	40.8730	51.6866	113.3267	155.5319
Remainder	5.0332	5.4542	6.6245	6.9740
Core	3.2600	3.2664	3.2793	3.2823
Total	−2.7742	110.0850	2896.7954	−477.2554

The most important polarizability is that of the $4s$ ground state and there is only a 1% variation between the DFCP, MBPT-SD, and CICP static dipole polarizabilities. The DFCP polarizability is smaller than the MBPT-SD polarizability because the DFCP $4s-4p_J$ matrix elements are smaller. The RCC calculation of the dipole polarizability is the clear outlier at 73.0 a.u. [26]. The good agreement between the DFCP, CICP, and MBPT-SD polarizabilities does not necessarily imply a 1% reliability in these polarizabilities since the calculations give lifetimes for the $4p_J$ states that are 2%–3% smaller than experiment.

The variation between the DFCP, MBPT-SD, and CICP estimates of the $3d_J$ state polarizabilities do not exceed 1.0 a.u. The difference in the polarizabilities for the two members of the spin-orbit doublet is only 0.2 a.u.

The polarizabilities of the $4p_J$ states are close to zero with the polarizability of the $4p_{3/2}$ state being about 1.8 a.u. larger than the polarizability of the $4p_{1/2}$ state. The polarizability

TABLE VIII. The contributions of individual transitions to the polarizabilities of the $4s_{1/2}$ and $4p_{3/2}$ states at the magic wavelengths. These results assume nonpolarized light. The numbers in parentheses are uncertainties in the last digits calculated by assuming certain matrix elements have ±2% uncertainties.

ω (a.u.) λ (nm)	0 ∞	0.066 320 4(11 651) 687.022(12.285)	0.114 992 3(4) 396.2315(13)	0.123 265 0(511) 369.6393(1534)	0.067 751 7(11 210) 672.508(11.3150)	0.115 125 1(3) 395.7748(10)
				$4s_{1/2}$		
$4p_{1/2}$	24.0704	36.1337	−6530.5659	−157.0218	36.9414	−4009.0830
$5p_{1/2}$	0.0097	0.0103	0.0117	0.0121	0.0103	0.0117
$4p_{3/2}$	47.7532	71.0638	3449.6093	−358.6372	72.6100	4129.0858
$5p_{3/2}$	0.0145	0.0154	0.0175	0.0181	0.0154	0.0175
Remainder	0.1672	0.1710	0.1794	0.1813	0.1712	0.1794
Core	3.2600	3.2664	3.2791	3.2820	3.2667	3.2792
Total	75.2751	110.6606	−3077.3881	−512.1655	113.0150	123.4906
				$4p_{3/2}$		
	Average	$m_j = 1/2$	$m_j = 1/2$	$m_j = 1/2$	$m_j = 3/2$	$m_j = 3/2$
$4s_{1/2}$	−11.9383	−71.0636	−3449.6902	358.6371	0.0000	0.0000
$5s_{1/2}$	6.0501	34.3769	219.9519	−1069.3049	0.0000	0.0000
$3d_{3/2}$	−5.4283	1.4608	0.2153	0.1808	11.6778	1.9317
$4d_{3/2}$	5.8429	1.0626	2.3512	3.2245	9.6796	21.2507
$3d_{5/2}$	−31.6965	77.2921	11.5779	9.7303	45.8671	7.6960
$4d_{5/2}$	33.7190	57.2196	126.3638	173.0763	38.6057	84.5964
Remainder	4.3193	7.0456	8.5623	9.0081	3.9179	4.7365
Core	3.2600	3.2664	3.2791	3.2820	3.2667	3.2792
Total	−4.1279	110.6606	−3077.3881	−512.1655	113.0150	123.4906

is small because the downward transitions to the $4s_{1/2}$ and $3d_J$ states have negative oscillator strengths which result in cancellations in the oscillator strength sum. This is evident in Tables VII and VIII, which show the breakdown of the different contributions to the polarizabilities from the oscillator strength sum rule.

The comparisons of the polarizabilities suggest that the basis set used in the RCC calculations [26] could be improved. The recommended results for the RCC calculation are those computed with the Gaussian basis. However, RCC calculations performed using a Slater-type orbital basis [26] give polarizabilities that are in much better agreement with the MBPT-SD and DFCP polarizabilities.

B. Dynamic polarizabilities and magic wavelengths

The dynamic dipole polarizability of a state at photon energy ω is defined

$$\alpha_1(\omega) = \sum_i \frac{f_{gi}^{(1)}}{\varepsilon_{gi}^2 - \omega^2}. \tag{12}$$

The dipole polarizability has a tensor component for states with states with $J > 1/2$. This can be written

$$\alpha_1^{\mathrm{T}}(\omega) = 6\left(\frac{5J_g(2J_g-1)(2J_g+1)}{6(J_g+1)(2J_g+3)}\right)^{1/2} \times \sum_{J_i}(-1)^{J_g+J_i}\begin{Bmatrix} J_g & 1 & J_i \\ 1 & J_g & 2 \end{Bmatrix}\frac{f_{gi}^{(1)}}{\varepsilon_{gi}^2-\omega^2}. \tag{13}$$

The polarizability for a state with nonzero angular momentum J depends on the magnetic projection M_g:

$$\alpha_{1,M_g} = \alpha_1 + \alpha_1^T \frac{3M_g^2 - J_g(J_g+1)}{J_g(2J_g-1)}. \tag{14}$$

The dynamic polarizabilities include contributions from the core which is represented by a pseudo-oscillator strength distribution [31,73,74] which is tabulated in Table IX. The distribution is derived from the single-particle energies of a Hartree-Fock core. Each separate (n,ℓ) level is identified with one transition with a pseudo-oscillator strength equal to the number of electrons in the shell. The excitation energy is set by adding a constant to the Koopmans energies and adjusting the constant until the core polarizability from the oscillator strength sum rule is equal to the known core polarizability of 3.26 a.u. The core polarizabilities of any two states effectively cancel each other when the polarizability differences are computed.

TABLE IX. Pseudospectral oscillator strength distribution used in the computation of the dynamic polarizability of the Ca^{2+} core. Energies are given in a.u.

i	ε_i	f_i
1	133.689 002	2.0
2	14.645 933	2.0
3	11.675 258	6.0
4	1.904 777 2	2.0
5	1.110 417 1	6.0

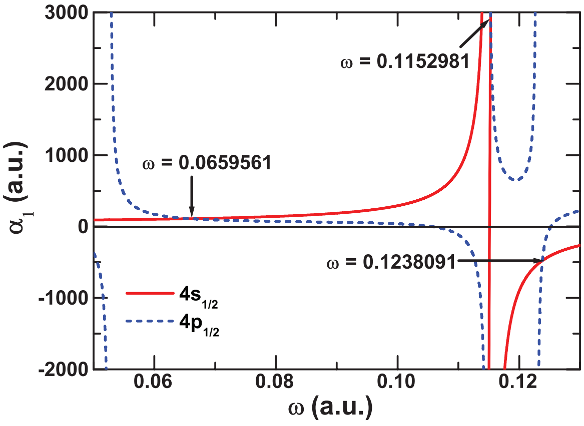

FIG. 1. (Color online) Dynamic polarizabilities of the $4s_{1/2}$ and $4p_{1/2}$ states of the Ca^+ ions. Magic wavelengths are identified by arrows.

The dynamic polarizabilities for the $4s_{1/2}$ and $4p_{1/2}$ states of Ca^+ are shown in Fig. 1. The first magic wavelength occurs at $\omega = 0.065\,956\,1$ a.u. after the photon wavelength exceeds the energy for the $4p_{1/2}$–$3d_{3/2}$ transition. Magic wavelengths are identified at $\lambda = 690.817$, 395.181, and 368.015 nm. The 395.181-nm magic wavelengths occur when the photon is very close to the excitation energies of the $4s$–$4p_J$ states. The 368.015-nm magic wavelength occurs near the energy for the $4p_{1/2}$–$5s_{1/2}$ transition. The dominant contributions to polarizabilities at the magic wavelengths are listed in

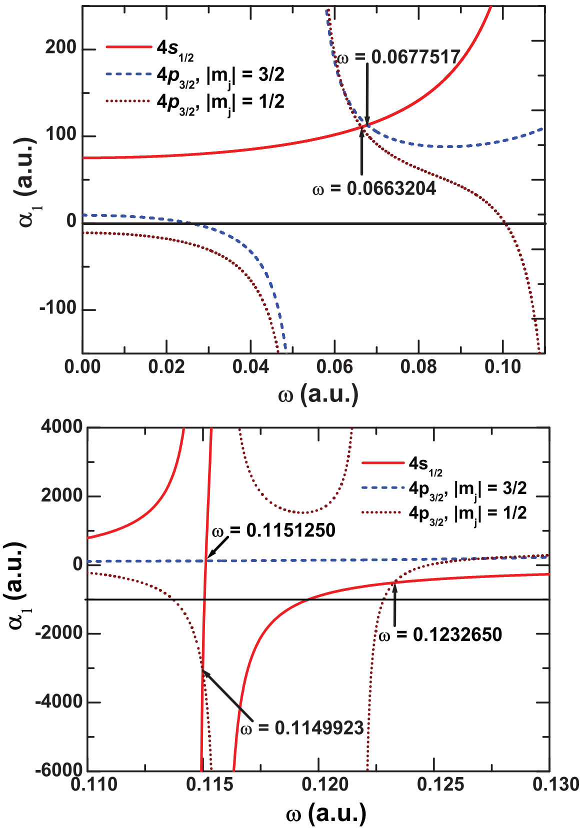

FIG. 2. (Color online) Dynamic polarizabilities of the $4s_{1/2}$ and $4p_{3/2}$ states of Ca^+. Magic wavelengths are identified by arrows.

Table VII. The $4s$ polarizability is dominated by the $4s_{1/2}-4p_J$ transitions with the next largest contribution coming from the core. However, the $4p_{1/2}$ polarizability has significant contributions from the transitions to the $4s$, $5s$, and $3d_{3/2}$ states. A magic wavelength experiment would give information about the $4p_{1/2}$ state, but would not give detailed information about any individual matrix element. An experiment that measured all three magic wavelengths could conceivably be able to extract information about individual line strengths; however, it should be noted that two of the transitions are in the ultraviolet.

The dynamic polarizabilities of the $4s_{1/2}$ and $4p_{3/2}$ states of Ca^+ are shown in Fig. 2. These figures assume nonpolarized light. Figure 2 only has two magic wavelengths below $\omega = 0.125$ a.u. Transitions to the $ns_{1/2}$ states make no contribution to the $4p_{3/2}$ state polarizability. This is evident from Table VIII, which details the breakdown of different transitions to the polarizability. The magic wavelength at 395.775 nm for the $4p_{3/2,m=3/2}$ magnetic sublevel can give an estimate of the contribution to the $np_{3/2}$ polarizability arising from excitations to the nd_J levels.

The $4s_{1/2}$ and $3d_{5/2}$ polarizabilities are shown in Figs. 3 and 4. The $3d_{5/2,m}$ polarizabilities are shown for all magnetic sublevels and also for the average polarizability. Magic wavelengths occur when the photon energy gets close to the excitation energies for the $3d_{5/2} \rightarrow 4p_J$ transitions and the $4s_{1/2} \rightarrow 4p_J$ transitions. Figure 3 shows the $4s_{1/2}$ and $3d_{5/2}$ polarizabilities at photon energies between 0.02 and 0.07 a.u. Precise values of the magic wavelengths and the breakdown of the polarizability into different components can be found in Table X.

Two of the magnetic sublevels have magic wavelengths at infrared frequencies, namely $\lambda = 1338.474$ and 1074.336 nm. The contributions to the in $3d_{5/2}$ polarizability are dominated by the $3d_{5/2} \rightarrow 4p_{3/2}$ transition which constitutes about 88% of the polarizability. The measurement of these magic wavelengths provides a method to determine the $f_{4s_{1/2}\rightarrow 4p_J}$ to $f_{3d_{5/2}\rightarrow 4p_{3/2}}$ oscillator strength ratios. Suppose all the remaining components of the $3d_{5/2}$ polarizability can only be estimated to an accuracy of 10%. The overall net uncertainty in the remaining terms would be less than 1.5%.

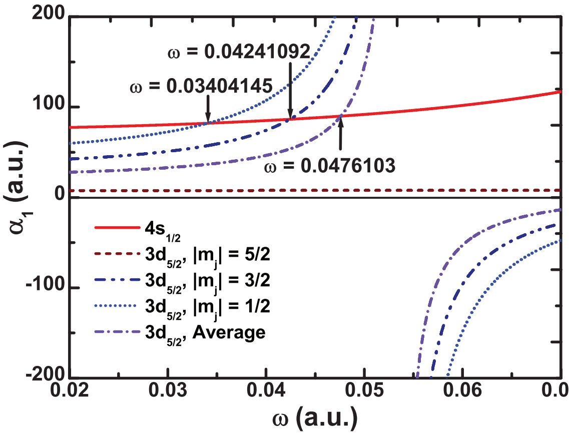

FIG. 3. (Color online) Dynamic polarizabilities of the $4s_{1/2}$ and $3d_{5/2}$ states of Ca^+. Magic wavelengths are identified by arrows.

There are additional magic wavelengths that can potentially be measured. The $4s$ dynamic polarizability goes through zero as the wavelength passes through energies needed to excite the $4s \rightarrow 4p_{1/2}$ and $4s \rightarrow 4p_{3/2}$ transitions. Figure 4 shows the polarizabilities for the $4s$ and $3d_{5/2}$ at energies near the $4s \rightarrow 4p_J$ excitation energies. The $3d_{5/2}$ polarizabilities are typically small in magnitude in this wavelength range. The magic wavelength arises more from the the cancellation of the

TABLE X. The contributions of individual transitions to the polarizabilities of the $4s_{1/2}$ and $3d_{5/2}$ states at the magic wavelengths. These results assume nonpolarized light. The numbers in parentheses are uncertainties in the last digits calculated by assuming certain matrix elements have ±2% uncertainties as described in the text.

ω (a.u.) λ (nm)	0 ∞	0.034 041 4(22 387) 1338.474(82.593)	0.042 410 9(10 654) 1074.336(26.352)	0.115 118 2(1) 395.7982(1)	0.115 118 4(1) 395.7978(1)	0.115 118 6(1) 395.7968(1)
			$4s_{1/2}$			
$4p_{1/2}$	24.0704	26.3917	27.8762	−4090.5249	−4088.7574	−4085.2247
$5p_{1/2}$	0.0097	0.0098	0.0099	0.0117	0.0117	0.0117
$4p_{3/2}$	47.7532	52.2705	55.1513	4087.5752	4088.4488	4090.2003
$5p_{3/2}$	0.0145	0.0147	0.0148	0.0175	0.0175	0.0175
Remainder	0.1672	0.1682	0.1688	0.1794	0.1794	0.1793
Core	3.2600	3.2618	3.2627	3.2792	3.2792	3.2792
Total	75.2751	82.1167	86.4837	0.5371	3.1792	8.4633
			$3d_{5/2}$			
	Average	$m_j = 1/2$	$m_j = 3/2$	$m_j = 1/2$	$m_j = 3/2$	$m_j = 5/2$
$4p_{3/2}$	29.5834	71.3309	76.6749	−11.5457	−7.6971	0.0000
$5p_{3/2}$	0.0113	0.0165	0.0119	0.0227	0.0151	0.0000
$4f_{5/2}$	0.0607	0.0109	0.0988	0.0136	0.1223	0.3398
$5f_{5/2}$	0.0196	0.0035	0.0318	0.0041	0.0367	0.1018
$4f_{7/2}$	2.5573	3.2582	2.7444	4.0780	3.3983	2.0391
$5f_{7/2}$	0.8270	1.0479	0.8799	1.2223	1.0186	0.6112
Remainder	2.5979	3.1870	2.7803	3.4628	3.0060	2.0922
Core	3.2600	3.2618	3.2627	3.2792	3.2792	3.2792
Total	38.5915	82.1167	86.4837	0.5371	3.1792	8.4633

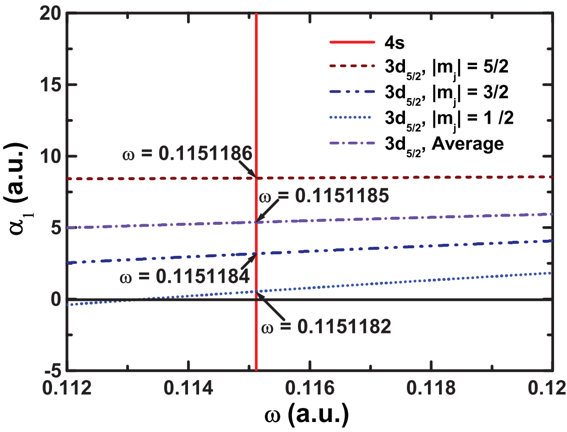

FIG. 4. (Color online) Dynamic polarizabilities of the $4s_{1/2}$ and $3d_{5/2}$ states of Ca$^+$. Magic wavelengths are identified by circles and arrows.

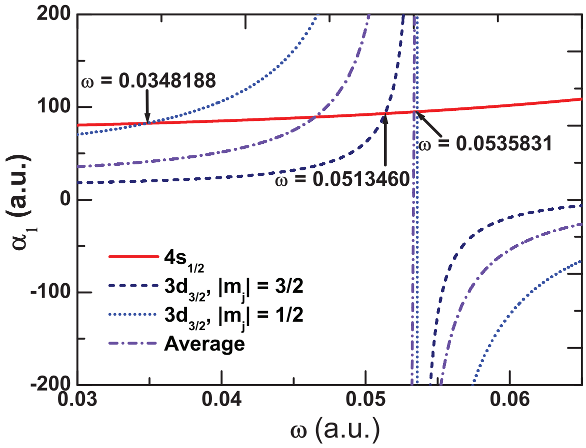

FIG. 5. (Color online) Dynamic polarizabilities of the $4s_{1/2}$ and $3d_{3/2}$ states of Ca$^+$. Magic wavelengths are identified by arrows.

$4p_{1/2}$ and $4p_{3/2}$ contributions to the $4s$ dynamic polarizability than from the cancellation between the $4s$ and $3d_{5/2}$ dynamic polarizabilities. Measurement of the magic wavelength here is in some respects analogous to a measurement of the longest tune-out wavelength for neutral potassium [56]. Zero field shift wavelengths measured in the spin-orbit energy gap of the resonant transition are strongly dominated by the large and opposite polarizability contributions of the two members of the spin-orbit doublet [56,75]. This makes it possible to accurately determine the oscillator strength ratio, i.e., $f_{4s\rightarrow 4p_{1/2}}$:$f_{4s\rightarrow 4p_{3/2}}$, of the two transitions comprising the spin-orbit doublet.

Table XI identifies the magic wavelengths associated with the $4s \rightarrow 3d_{3/2}$ energy interval. The situation here is similar to the situation for the $4s \rightarrow 3d_{5/2}$ magic wavelengths. However, there are three magic wavelengths in the infrared region of the spectrum. This transition has an additional magic wavelength since the $3d_{3/2,m=1/2}$ state, unlike the $3d_{5/2,m=1/2}$ state, also undergoes undergoes a transition to the $4p_{1/2}$ state. The polarizability difference in the 0.02- to 0.07-a.u. energy range is plotted in Fig. 5. The $3d_{3/2}$ polarizability is dominated by the $3d_{3/2} \rightarrow 4p_J$ transition and a magic wavelength measurement can be used to make an estimate of the $3d_{3/2} \rightarrow 4p_J$ line strength relative to the $4s$ dynamic polarizability. The $3d_{3/2,m=1/2}$ polarizability at 850.335 nm has large contributions from the $4p_{1/2}$ and $4p_{3/2}$ states since it lies between the excitation energies of these of states. Measurement of the 850.335- and 1308.590-nm wavelengths together would give estimates of the $3d_{3/2} \rightarrow 4p_{1/2}$ line

TABLE XI. The contributions of individual transitions to the polarizabilities of the $4s_{1/2}$ and $3d_{3/2}$ states at the magic wavelengths. These results assume nonpolarized light. The numbers in parentheses are uncertainties in the last digits calculated by assuming certain matrix elements have ±2% uncertainties as described in the text.

ω	0	0.034 818 8(20 007)	0.051 346 0(1855)	0.053 583 1(1)	0.115 118 2(1)	0.115 118 5(1)
λ	∞	1308.590(71.108)	887.382(3.196)	850.335(2)	395.7981(1)	395.7970(1)
				$4s_{1/2}$		
$4p_{1/2}$	24.0704	26.5098	30.0922	30.7777	−4090.1007	−4086.1347
$5p_{1/2}$	0.0097	0.0098	0.0100	0.0101	0.0117	0.0117
$4p_{3/2}$	47.7532	52.4999	59.4402	60.7642	4087.7840	4089.7488
$5p_{3/2}$	0.0145	0.0147	0.0150	0.0151	0.0175	0.0175
Remainder	0.1672	0.1683	0.1695	0.1697	0.1794	0.1794
core	3.2600	3.2619	3.2639	3.2643	3.2792	3.2792
Total	75.2751	82.4644	92.9908	95.0011	1.1711	7.1019
				$3d_{3/2}$		
	Average	$m_j = 1/2$	$m_j = 3/2$	$m_j = 1/2$	$m_j = 1/2$	$m_j = 3/2$
$4p_{1/2}$	9.9038	70.5419	0	−1034.8996	−10.4461	0
$5p_{1/2}$	0.0033	0.0134	0	0.0139	0.0184	0
$4p_{3/2}$	5.4284	1.3416	84.7097	1119.1728	−0.2147	−1.9320
$5p_{3/2}$	0.0021	0.0003	0.0029	0.0003	0.0004	0.0038
$4f_{5/2}$	2.3339	3.1745	2.1676	3.2644	3.9674	2.6449
$5f_{5/2}$	0.7556	1.0218	0.6928	1.0422	1.1908	0.7939
Remainder	2.3601	3.1091	2.1539	3.1428	3.3757	2.3121
core	3.2600	3.2619	3.2639	3.2643	3.2792	3.2792
Total	24.0472	82.4644	92.9908	95.0011	1.1711	7.1019

strengths and the $f_{3d_{3/2}\rightarrow 4p_{1/2}}$:$f_{3d_{3/2}\rightarrow 4p_{3/2}}$ ratio. A measurement of the magic wavelengths in the vicinity 395 nm provides would permit a determination of the $f_{4s\rightarrow 4p_{1/2}}$:$f_{4s\rightarrow 4p_{3/2}}$ ratio.

C. Uncertainties

An uncertainty analysis has been done for all the magic wavelengths presented in the preceding sections. This analysis was aimed at making an initial estimate of how uncertainties in the matrix elements of the most important transitions would translate to a shift in the magic wavelengths. The primary purpose of the uncertainty analysis is to define reasonable limits to help guide an experimental search for the magic wavelengths identified in this paper.

In the case of the $4s \rightarrow 4p_J$ polarizability differences, the $4s \rightarrow 4p_J$, $4p_J \rightarrow 5s$, $4p_J \rightarrow 3d_J$, and $4p_J \rightarrow 4d_J$ matrix elements were all changed by 2% and the magic wavelengths recomputed. The matrix elements involving the different spin-orbit states of the same multiplet were all given the same scaling. A variation of ±2% was chosen by reference to the difference of the DFCP matrix elements with the experimental or the MBPT-SD matrix elements. The estimate of a 2% uncertainty in the $4s \rightarrow 4p_J$ matrix element can be regarded as a conservative estimate.

The $4s \rightarrow 3d_J$ polarizability difference is predominantly determined by the $4s \rightarrow 4p_J$ and $3d_J \rightarrow 4p_J$ matrix elements. So variations of ±2% in these two transitions were used in determining the uncertainties in the magic wavelengths.

There are a number of magic wavelengths which are relatively insensitive to changes in the matrix elements of a multiplet. One of these wavelengths is the 850-nm wavelength for the $4s{-}3d_{3/2}$ interval and the others are the magic wavelengths near 395 nm. These wavelengths arise due to cancellations in the polarizabilities due to two transitions of a spin-orbit doublet. In the case of the 850-nm magic wavelength, the relevant transitions are the $3d_{3/2} \rightarrow 4p_J$ transitions.

The sensitivity of the magic wavelengths near 395 nm to changes in the transition matrix elements depends on the overall size of the polarizabilities of the $4p_J$ and $3d_J$ levels. When these are large due to transitions other than the $4s \rightarrow 4p_J$ transition, then the 395-nm magic wavelength shows higher sensitivity to the changes in the matrix elements. However, the net change in the magic wavelengths for 2% changes in the matrix elements is about 0.001 nm for the $4s \rightarrow 4p_J$ interval. The sensitivity to 2% matrix element changes for the $4s \rightarrow 3d_J$ intervals is about 0.0001 nm due to the small polarizabilities of the $3d_J$ states near 395 nm. The 850-nm magic wavelength is also relatively insensitive to changes in the overall size of the matrix elements, with the 2% matrix element change leading to a change of only 0.0001 nm in the magic wavelengths. The low sensitivity of magic wavelengths to the overall size of the matrix elements in these cases means that these the magic wavelengths can be used to give precise estimates of the matrix element ratios of the two transitions in the spin-orbit doublet.

The 1338-, 1309-, 1074-, 887-nm magic wavelengths show much greater sensitivity to 2% changes in the matrix elements. The changes in the magic wavelengths range from 3 to 80 nm. The sensitivity of the magic wavelengths to these matrix elements is driven by the rate of change of the $4s$ and $3d_J$ polarizabilities with energy. A large change in the photon energy is needed to compensate for a small change in the polarizability when $d\alpha_1/d\omega$ is small. The sensitivity of the magic wavelength to small changes in the matrix elements decreases as the photon energy gets closer to the $3d_J \rightarrow 4p_{J'}$ excitation thresholds. The high sensitivity of the magic wavelengths with respect to changes in the matrix elements means it is only necessary to measure the magic wavelength to a precision of 0.10 nm to impose reasonably tight constraints on the ratios of the $4s \rightarrow 4p_J$ and $3d_J \rightarrow 4p_{J'}$ matrix element rations.

V. CONCLUSION

A relativistic semiempirical core model is applied to the calculation of the dynamic polarizabilities of the $4s$, $3d_J$, and $4p_J$ states of Ca$^+$. A number of magic wavelengths at convenient photon energies have been identified for the $4s{-}3d_J$ energy intervals. Measurement of these magic wavelengths can be used to determine reasonably accurate estimates of the $3d_J$-$4p_{J'}$ line strengths relative to the $4s{-}4p_J$ line strengths. This could lead to improved estimates of the blackbody radiation shift for the Ca$^+$ clock transition. There is one impediment. At the moment there is a 3% spread between theoretical and experimental lifetimes for the $4p_{J'}$ states. This variation, which does not exist for the same transition in potassium [56,76], needs to be resolved so the uncertainty in the $4s{-}4p_J$ line strengths can be reduced to 1% or better.

There are two other relatively clean measurements of atomic structure parameters that could be made. Measurement of the magic wavelength near 395 nm could be used to determine a value of the oscillator strength $f_{4s\rightarrow 4p_{1/2}}$:$f_{4s\rightarrow 4p_{3/2}}$ ratio. This could help resolve the incompatible predictions of this ratio by DFCP/MBPT-SD and RCC calculations. Comparisons of polarizabilities do suggest that the Gaussian basis set used for the RCC calculations could be improved. Further, measurements of the two longest magic wavelengths for the $3d_{3/2,m=1/2} \rightarrow 4s_{1/2}$ transition could give a good estimate of the $f_{3d_{3/2}\rightarrow 4p_{1/2}}$:$f_{3d_{3/2}\rightarrow 4p_{3/2}}$ ratio.

The utility of measuring magic wavelengths for selected Ca$^+$ transitions can of course be extended to other alkaline-earth ions, with Sr$^+$ and Ba$^+$ being obvious possibilities. A single-ion optical frequency standard at the 10^{-17} level of precision has recently been reported for the $5s{-}4d_{5/2}$ transition of the Sr$^+$ ion [77]. It is likely that the determination of the magic wavelengths for this transition could be used to improve the precision of estimates of the blackbody radiation shift for this transition [57,78].

ACKNOWLEDGMENTS

This work was supported by the National Basis Research Program of China under Grants No. 2010CB832803 and No. 2012CB821305 and by NNSF of China under Grants No. 11274348 and No. 11034009. This research was supported by Australian Research Council Discovery Project No. DP-1092620. We would like to thank Dr. Jun Jiang of CDU for assistance in manuscript preparation.

[1] T. M. Miller and B. Bederson, Adv. At. Mol. Phys. **13**, 1 (1977).
[2] K. D. Bonin and V. V. Kresin, *Electric Dipole Polarizabilities of Atoms, Molecules and Clusters* (World Scientific, Singapore, 1997).
[3] J. Mitroy, M. S. Safronova, and C. W. Clark, J. Phys. B **43**, 202001 (2010).
[4] H. Katori, M. Takamoto, V. G. Pal'chikov, and V. D. Ovsiannikov, Phys. Rev. Lett. **91**, 173005 (2003).
[5] R. Santra, K. V. Christ, and C. H. Greene, Phys. Rev. A **69**, 042510 (2004).
[6] B. Arora, M. S. Safronova, and C. W. Clark, Phys. Rev. A **76**, 052509 (2007).
[7] M. S. Safronova, U. I. Safronova, and C. W. Clark, Phys. Rev. A **86**, 042505 (2012).
[8] A. Bauch, Meas. Sci. Technol. **14**, 1159 (2003).
[9] M. Takamoto and H. Katori, Phys. Rev. Lett. **91**, 223001 (2003).
[10] P. Gill, Metrologia **42**, S125 (2005).
[11] L. Lorini, N. Ashby, A. Brusch, S. Diddams, R. Drullinger, E. Eason, T. Fortier, P. Hastings, T. Heavner, D. Hume *et al.*, Eur. Phys. J. Spec. Top. **163**, 19 (2008).
[12] P. Gill, Philos. Trans. R. Soc., A **369**, 4109 (2011).
[13] S. G. Porsev, A. D. Ludlow, M. M. Boyd, and J. Ye, Phys. Rev. A **78**, 032508 (2008).
[14] C. D. Herold, V. D. Vaidya, X. Li, S. L. Rolston, J. V. Porto, and M. S. Safronova, Phys. Rev. Lett. **109**, 243003 (2012).
[15] L. J. LeBlanc and J. H. Thywissen, Phys. Rev. A **75**, 053612 (2007).
[16] B. Arora, M. S. Safronova, and C. W. Clark, Phys. Rev. A **84**, 043401 (2011).
[17] W. F. Holmgren, R. Trubko, I. Hromada, and A. D. Cronin, Phys. Rev. Lett. **109**, 243004 (2012).
[18] J. McKeever, J. R. Buck, A. D. Boozer, A. Kuzmich, H.-C. Nagerl, D. M. Stamper-Kurn, and H. J. Kimble, Phys. Rev. Lett. **90**, 133602 (2003).
[19] C. Degenhardt, H. Stoehr, U. Sterr, F. Riehle, and C. Lisdat, Phys. Rev. A **70**, 023414 (2004).
[20] F. L. Kien, V. I. Balykin, and K. Hakuta, J. Phys. Soc. Jpn. **74**, 910 (2005).
[21] Z. W. Barber, J. E. Stalnaker, N. D. Lemke, N. Poli, C. W. Oates, T. M. Fortier, S. A. Diddams, L. Hollberg, C. W. Hoyt, A. V. Taichenachev *et al.*, Phys. Rev. Lett. **100**, 103002 (2008).
[22] L. Yi, S. Mejri, J. J. McFerran, Y. Le Coq, and S. Bize, Phys. Rev. Lett. **106**, 073005 (2011).
[23] A. Kreuter, C. Becher, G. P. T. Lancaster, A. Mundt, C. Russo, H. Haffner, C. Roos, W. Hansel, F. Schmidt-Kaler, R. Blatt *et al.*, Phys. Rev. A **71**, 032504 (2005).
[24] J. Mitroy and J. Y. Zhang, Eur. Phys. J. D **46**, 415 (2008).
[25] D. Jiang, B. Arora, and M. S. Safronova, Phys. Rev. A **78**, 022514 (2008).
[26] B. K. Sahoo, B. P. Das, and D. Mukherjee, Phys. Rev. A **79**, 052511 (2009).
[27] B. Arora, M. S. Safronova, and C. W. Clark, Phys. Rev. A **76**, 064501 (2007).
[28] M. S. Safronova, W. R. Johnson, and U. I. Safronova, J. Phys. B **43**, 074014 (2010).
[29] M. S. Safronova and U. I. Safronova, Phys. Rev. A **83**, 012503 (2011).
[30] J. Mitroy, D. C. Griffin, D. W. Norcross, and M. S. Pindzola, Phys. Rev. A **38**, 3339 (1988).
[31] J. Mitroy and M. W. J. Bromley, Phys. Rev. A **68**, 052714 (2003).
[32] J. Mitroy and M. S. Safronova, Phys. Rev. A **79**, 012513 (2009).
[33] J. Mitroy, J. Y. Zhang, M. W. J. Bromley, and K. G. Rollin, Eur. Phys. J. D **53**, 15 (2009).
[34] N. Vaeck, M. Godefroid, and C. Froese Fischer, Phys. Rev. A **46**, 3704 (1992).
[35] J. Mitroy, J. Phys. B **26**, 2201 (1993).
[36] I. P. Grant, *Relativistic Quantum Theory of Atoms and Molecules Theory and Computation* (Springer, New York, 2007).
[37] C. C. Roothaan, Rev. Mod. Phys. **23**, 69 (1951).
[38] J. Mitroy, Aust. J. Phys. **52**, 973 (1999).
[39] W. R. Johnson, S. A. Blundell, and J. Sapirstein, Phys. Rev. A **37**, 307 (1988).
[40] L. Y. Tang, Y. H. Zhang, X. Z. Zhang, J. Jiang, and J. Mitroy, Phys. Rev. A **86**, 012505 (2012).
[41] Y. Tang, Z. Zhong, C. Li, H. Qiao, and T. Shi, Phys. Rev. A **87**, 022510 (2013).
[42] F. A. Parpia, C. Froese Fischer, and I. P. Grant, Comp. Phys. Commun. **94**, 249 (1996).
[43] A. Kramida, Y. Ralchenko, J. Reader, and NIST ASD Team, NIST Atomic Spectra Database (version 5.0.0) (2012), http://physics.nist.gov/asd.
[44] S. Hameed, A. Herzenberg, and M. G. James, J. Phys. B **1**, 822 (1968).
[45] S. Hameed, J. Phys. B **5**, 746 (1972).
[46] W. R. Johnson, D. Kolb, and K. Huang, At. Data Nucl. Data Tables **28**, 333 (1983).
[47] M. S. Safronova, A. Derevianko, and W. R. Johnson, Phys. Rev. A **58**, 1016 (1998).
[48] R. Pal, M. S. Safronova, W. R. Johnson, A. Derevianko, and S. G. Porsev, Phys. Rev. A **75**, 042515 (2007).
[49] M. S. Safronova and W. R. Johnson, Adv. At. Mol. Opt. Phys. **55**, 191 (2008).
[50] S. G. Porsev, M. S. Safronova, and M. G. Kozlov, Phys. Rev. A **85**, 062517 (2012).
[51] L. W. Wansbeek, B. K. Sahoo, R. G. E. Timmermans, B. P. Das, and D. Mukherjee, Phys. Rev. A **78**, 012515 (2008).
[52] L. W. Wansbeek, B. K. Sahoo, R. G. E. Timmermans, B. P. Das, and D. Mukherjee, Phys. Rev. A **82**, 029901(E) (2010).
[53] J. Mitroy, J. Y. Zhang, and K. Varga, Phys. Rev. Lett. **101**, 123201 (2008).
[54] B. K. Sahoo, M. R. Islam, B. P. Das, R. K. Chaudhuri, and D. Mukherjee, Phys. Rev. A **74**, 062504 (2006).
[55] B. Arora, D. K. Nandy, and B. K. Sahoo, Phys. Rev. A **85**, 012506 (2012).
[56] J. Jiang, L. Y. Tang, and J. Mitroy, Phys. Rev. A **87**, 032518 (2013).
[57] J. Mitroy, J. Y. Zhang, and M. W. J. Bromley, Phys. Rev. A **77**, 032512 (2008).
[58] J. Lidberg, A. Al-Khalili, L.-O. Norlin, P. Royen, X. Tordoir, and S. Mannervik, J. Phys. B **32**, 757 (1999).
[59] T. Gudjons, B. Hilbert, P. Seibert, and G. Werth, Europhys. Lett. **33**, 595 (1996).
[60] M. Knoop, M. Vedel, and F. Vedel, Phys. Rev. A **52**, 3763 (1995).
[61] K. Matsubara, K. Hayasaka, Y. Li, H. Ito, S. Nagano, M. Kajita, and M. Hosokawa, Appl. Phys. Express **1**, 067011 (2008).
[62] M. Chwalla, J. Benhelm, K. Kim, G. Kirchmair, T. Monz, M. Riebe, P. Schindler, A. S. Villar, W. Hänsel, C. F. Roos *et al.*, Phys. Rev. Lett. **102**, 023002 (2009).
[63] Y. Huang, Q. Liu, J. Cao, B. Ou, P. Liu, H. Guan, X. Huang, and K. Gao, Phys. Rev. A **84**, 053841 (2011).

[64] Y. Huang, J. Cao, P. Liu, K. Liang, B. Ou, H. Guan, X. Huang, T. Li, and K. Gao, Phys. Rev. A **85**, 030503 (2012).

[65] K. Matsubara, H. Hachisu, Y. Li, S. Nagano, C. Locke, A. Nogami, M. Kajita, K. Hayasaka, T. Ido, and M. Hosokawa, Opt. Express **20**, 22034 (2012).

[66] J. Jin and D. A. Church, Phys. Rev. Lett. **70**, 3213 (1993).

[67] R. N. Gosselin, E. H. Pinnington, and W. Ansbacher, Phys. Rev. A **38**, 4887 (1988).

[68] A. Gallagher, Phys. Rev. **157**, 24 (1967).

[69] F. H. K. Rambow and L. D. Schearer, Phys. Rev. A **14**, 1735 (1976).

[70] R. Gerritsma, G. Kirchmair, F. Zähringer, J. Benhelm, R. Blatt, and C. F. Roos, Eur. Phys. J. D **50**, 13 (2008).

[71] B. K. Sahoo, Chem. Phys. Lett. **448**, 144 (2007).

[72] E. S. Chang, J. Phys. B **16**, L539 (1983).

[73] D. J. Margoliash and W. J. Meath, J. Chem. Phys. **68**, 1426 (1978).

[74] A. Kumar and W. J. Meath, Mol. Phys. **54**, 823 (1985).

[75] L. Y. Tang, M. W. J. Bromley, Z. C. Yan, and J. Mitroy, Phys. Rev. A **87**, 032507 (2013).

[76] U. I. Safronova and M. S. Safronova, Phys. Rev. A **78**, 052504 (2008).

[77] A. A. Madej, P. Dubé, Z. Zhou, J. E. Bernard, and M. Gertsvolf, Phys. Rev. Lett. **109**, 203002 (2012).

[78] D. Jiang, B. Arora, M. S. Safronova, and C. W. Clark, J. Phys. B **42**, 154020 (2009).